Environmental Science and Pollution Research (2023) 30:41537–41552
https://doi.org/10.1007/s11356-023-25159-6

RESEARCH ARTICLE

An improved algorithm for estimating the Secchi disk depth of inland waters across China based on Sentinel-2 MSI data

Zihong Qin[1] · **Youyue Wen**[2] · **Jiegui Jiang**[3] · **Qiang Sun**[2]

Received: 10 August 2022 / Accepted: 1 January 2023 / Published online: 12 January 2023

Abstract

Accurate remote sensing of the Secchi disk depth (Z_{SD}) in waters is beneficial for large-scale monitoring of the aquatic ecology of inland lakes. Herein, an improved algorithm (termed as Z_{SD20} in this work) for retrieving Z_{SD} was developed from field measured remote sensing data and is available for various waters including clear waters, slightly turbid waters, and highly turbid waters. The results show that Z_{SD20} is robust in estimating Z_{SD} in various inland waters. After further validation with an independent in situ dataset from 12 inland waters ($0.1\ \text{m} < Z_{SD} < 18\ \text{m}$), the developed algorithm outperformed the native algorithm, with the mean absolute square percentage error (MAPE) reduced from 32.8 to 19.4%, and root mean square error (RMSE) from 0.87 to 0.67 m. At the same time, the new algorithm demonstrates its generality in various mainstreaming image data, including Ocean and Land Color Instrument (OLCI), Geostationary Ocean Color Imager (GOCI), and Moderate Resolution Imaging Spectroradiometer (MODIS). Finally, the algorithm's application was implemented in 410 waters of China based on Sentinel-2 MSI imagery to elucidate the spatiotemporal variation of water clarity during 2015 and 2021. The new algorithm reveals great potential for estimating water clarity in various inland waters, offering important support for protection and restoration of aquatic environments.

Keywords Water clarity · Inland waters · Remote sensing · Semi-analytical model

Introduction

Water clarity is an integrative record of overall water quality and a convenient indicator for assessing trophic status in aquatic sciences and has been routinely and widely measured with Secchi disk (Z_{SD}, m) (Bai et al. 2020; Lee et al. 2016; Shi et al. 2018; Zhao et al. 2011). The Z_{SD} values depend on the intensity light and optically active constituents (e.g., chlorophyll-a, total suspended matter, and color dissolved organic matter) and play a critical role in understanding aquatic environment variations and biochemical processes (Feng et al. 2019; Song et al. 2021). Z_{SD} is also useful to monitor other bio-optical properties, such as the light availability for photo-synthetically active radiation (PAR), relating to its measurement costs and simplicity (Song et al. 2017; Zhang et al. 2012).

Over the past few decades, remote satellite data has also been used for estimating Z_{SD} due to its large coverage characteristics and rapid data acquisition (Fukushima et al. 2017; Mu et al. 2021; Olmanson et al. 2016; Shang et al. 2016). Generally, there are two strategies for retrieving Z_{SD} from remote sensing data: empirical and semi-analytical approaches. The empirical approaches usually estimate Z_{SD} by developing a regression model between field measured Z_{SD} and remote sensing reflectance (Binding et al. 2015; Olmanson et al. 2016; Shi et al. 2018). However, the empirical approaches have characteristic of site-specific limitation and may not be transferable to other settings (Lee et al. 2016; Ren et al. 2018; Xu et al. 2021a). In contrast, previous studies have confirmed that semi-analytical methods contain greater potential in developing a general approach for estimating Z_{SD} (Rodrigues et al. 2017; Yang et al. 2013). Therefore, semi-analytical algorithms generally provide more reliable results for monitoring the Z_{SD} in various aquatic ecosystems.

Responsible Editor: Marcus Schulz

✉ Qiang Sun
jydlzs@163.com

[1] School of Geography and Planning, Nanning Normal University, Nanning 530001, China

[2] Ministry of Ecology and Environment, South China Institute of Environmental Science, Guangzhou 510535, China

[3] School of Urbanism and Architecture, Guangzhou Huali College, Guangzhou 510535, China

An innovative semi-analytical model (termed as Z_{SDV6}) based on radiative transfer theory was proposed by Lee et al. (2015), and its superior performance was confirmed by subsequent studies (Lee et al. 2016; Shang et al. 2016). However, several defects may exist when applying the original algorithm to various settings with various optical properties. Firstly, the estimation of the total absorption coefficients at reference wavebands does not work in highly turbid waters due to large uncertainties in estimating total absorption coefficients (Liu et al. 2020; Mishra et al. 2014; Watanabe et al. 2016; Xue et al. 2019). Secondly, the coefficients of the original model, determined by open ocean and coastal water datasets, may produce over/underestimated inherent optical properties (IOPs). The third potential concern was that a fixed ratio value of 1.5 was assumed between beam radiance diffuse attenuation coefficient (c) and K_d (i.e., $K_T/K_d = 1.5$). Therefore, challenges remain for applying algorithms to estimate Z_{SD} in various waters, especially in large-scale applications.

Designed to provide continuous observations similar to the Landsat series, the MultiSpectral Instrument (MSI) onboard the twin satellites (Sentinel-2A and 2B), were launched by the European Space Agency Copernicus program in June 2015 and March 2017, respectively. With its eight bands from visible to shortwave infrared (SWIR) spectral region (443 ~ 835 nm) and fine temporal resolutions (5 days), the sentinel-2 MSI data has been considered as a superior satellite sensor with high signal-to-noise ratios (SNR) for regular estimation of target land-cover change at regional or global scales. Furthermore, with finer spatial resolution (10 m, 20 m, and 60 m) from visible to near-infrared (NIR) bands, MSI data provides more opportunities for enhanced monitoring of water quality parameters in smaller inland waters (e.g., water area < 30 km^2). However, the systematic spatiotemporal variation patterns of Z_{SD} using the above-mentioned satellite data on a large scale (e.g., national scale) have rarely been investigated.

Therefore, the main purposes of this study are to (1) provide an improved scalable semi-analytical model for estimating Z_{SD} in inland waters with various turbid categories; (2) validate a developed model and compare it with existing models; (3) demonstrate long-term applications of the developed model on a national scale using sentinel-2 MSI data.

Study area and data collection

Study area

Our surveyed area across China was divided into six large sub-regions, the Northeast Plain (NP) and Mountains (NE), Eastern Plain (EP), Inner-Mongolian Plateau (MP), Yunnan-Guizhou Plateau (YG), Xinjiang province (XJ), and Tibetan-Qinghai Plateau (TP) according to geographical conditions and climatic characteristics (Zhang et al. 2019). The sampled waters included 20 inland lakes that ranged from clear to highly turbid, from shallow to deep, and from oligotrophic to hypereutrophic (Fig. 1). These sampled lakes are sporadically distributed from the eastern region (NP and EP) to the western region (TP and XJ), with altitudes ranging from below 5 to above 4250 m. The basic information of 20 sampled lakes is shown in Fig. 1 and Table 1. Among the surveyed lakes, hypereutrophic lakes (e.g., Lake Taihu) are mainly located in the EP, while mesotrophic lakes (e.g., Lake Erhai) are mostly distributed in YG and EP. With the exception of Wanlv Lake in EP, most oligotrophic lakes are located on the TP, which are characterized by small water surface (< 30 km^2) and limited human disturbance.

In situ water quality data and spectra data collection

The dataset I (calibration)

From 2015 to 2021, water samples were collected by taking a total of 276 samples from ten lakes (Fig. 1 and Table 1). In situ surface water samples (~ 0.5 m depth) were measured using pre-cleaned Niskin bottles and were placed in an ice bin at low temperatures (~ 3 °C) for laboratory analysis. The measurements of water clarity (Z_{SD}, m) were simultaneously taken using a Secchi disk (Li et al. 2020; Ren et al. 2018). The Secchi disk is slowly lowered into a water column until it disappears from the inspector's view, the depth at which it is no longer visible is recorded as the Z_{SD} value (Zeng et al. 2020a). Within the following days, water samples were filtered and four water quality parameters, including concentration of total phosphorus (C_{TP}), chlorophyll-a (C_{Chla}), total suspended matter (C_{TSM}), and the absorption coefficients of colored dissolved organic matter (CDOM) at 443 nm (termed as $a_{CDOM}(443)$) were measured in the laboratory following the method described by Zeng et al. (2022a) and Xu et al. (2018a). At the same time, the trophic state of sampling lakes was evaluated by the Carlson's trophic state index (TSI) (Carlson 1977); the results are shown in Fig. 1 and Table 1.

The corresponding $R_{rs}(\lambda)$ was field-measured using an Analytical Spectral Devices (ASD) Inc. FieldSpec Pro between 14:00 and 16:00. More details of the process are provided by previous studies (Cai et al. 2021; Lei et al. 2018; Xu et al. 2020, 2021c). At each sampling point, the total radiance (L_t), the sky-viewing radiance (L_{sky}), and the radiance reflected by a standard gray panel (L_p) were collected. The $R_{rs}(\lambda)$ can be calculated using the following equation:

$$R_{rs}(\lambda) = \rho_p\left(L_t - r_{aw}L_{sky}\right)/(\pi Lp) \quad (1)$$

where r_{aw} represents the skylight reflectance at the air–water surface and is taken as 2.2% for calm water conditions (Zeng et al. 2022b; Zheng et al. 2016).

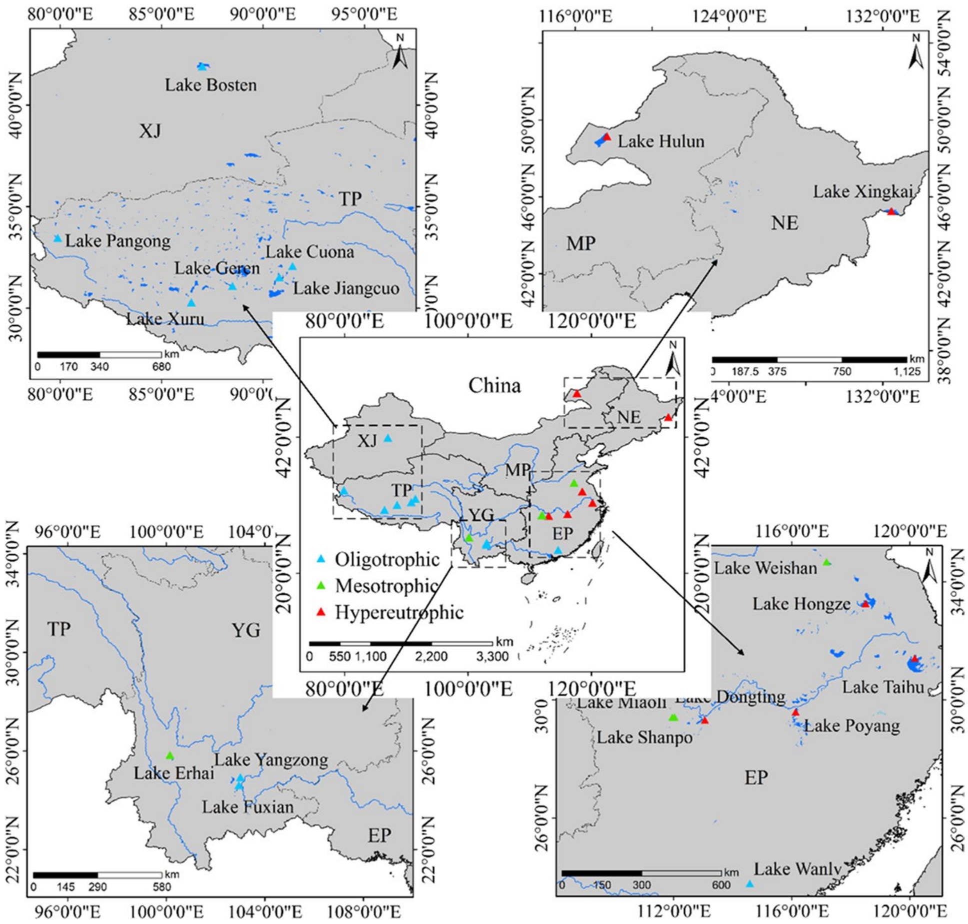

Fig. 1 Location of 20 sampling lakes. The blue, green, and red triangles mark the oligotrophic, mesotrophic, and hypereutrophic lakes, respectively

An underwater spectroradiometer (TriOS Mess- und Datentechnik GmbH, Rastede, Germany) was used to collect the diffuse attenuation coefficient $K_\mathrm{d}(\lambda)$ on site, which has a scanning channels range of 320 to 950 nm and a spectral sampling interval of 3.3 nm. After that, the spectral sampling interval can be interpolated to a narrow resolution of 1 nm through indoor data processing. The spectra of underwater downward irradiance $E_d(\lambda, z)$ at different sampling depths (z= 0.4, 0.8,…….,3.6 m) were measured following the methods suggested by Lei et al. (2020), and the $K_\mathrm{d}(\lambda)$ was calculated using a non-linear fit equation as follows:

$$E_d(\lambda, z) = E_d(\lambda, 0^-) * \exp\left(-K_\mathrm{d}(\lambda) * z\right) \tag{2}$$

$K_\mathrm{d}(\lambda)$ was determined only if $R^2 \geq 0.95$ and the number of sampling depths must be more than 3 (Zhang et al. 2012).

The dataset II (validation)

Another dataset (dataset II), including Z_SD and $R_{rs}(\lambda)$ measurements from 14 lakes, was collected by taking a total of 203 samples from 2015 to 2018 (Fig. 1, Table 1), similar protocols used for dataset I were followed. Notice that dataset II is used as an independent dataset for algorithm verification. The distributions of those water samples covered the eastern region to the southwest region (Yunnan Province and Tibet Plateau) in China (Fig. 1).

Water type classification

We divided waterbodies into three basic types determined by the shape of R_{rs}, and a simple but robust water type classification algorithm proposed by Balasubramanian et al. (2020) was applied in this study. According to Balasubramanian et al. (2020), if $R_{rs}(665) < R_{rs}(560)$ and $R_{rs}(665) > R_{rs}(490)$, the waterbodies were identified as slightly turbid waters (ST); if $R_{rs}(665) > R_{rs}(560)$ and $R_{rs}(740) > 0.01/\mathrm{sr}$, the waterbodies were classified as highly turbid waters (HT); if $R_{rs}(665) < R_{rs}(490)$, the waterbodies were identified as clear waters (CW). Finally, there were 120, 84, and 72 samples in dataset I classified into HT, ST, and CW, respectively, while 90, 52, and 61 samples were correspondingly classified in dataset II.

Table 1 The basic information of sampling lake is listed, including sampling number, date, central longitude (Lon.), central latitude (Lat.), water area (Area, m^2), and trophic status between 2015 and 2021

	Lake	Samples	Date	Lon	Lat	Area	Trophic state
Dataset I	Dongting	35	201,710	113.12	29.34	2579	Hypereutrophic
	Taihu	30	201,910	120.19	31.52	2348	Hypereutrophic
	Hulun	20	201,509	117.65	49.16	2339	Hypereutrophic
	Hongze	30	201,810	118.54	33.12	2069	Hypereutrophic
	Bosten	10	201,710	87	41.92	1646	Oligotrophic
	Wanlv	60	201,607	114.58	23.79	370	Oligotrophic
	Erhai	31	201,609	100.18	25.84	256.5	Mesotrophic
	Xingkai	10	201,509	132.45	45.26	148	Hypereutrophic
	Weishan	30	202,109	117.17	34.69	1266	Mesotrophic
	Maoli	20	202,109	111.94	29.42	38.4	Mesotrophic
Dataset II	Poyang	34	201,808	116.67	29.14	3150	Hypereutrophic
	Erhai	30	201,810	100.18	25.84	256.5	Mesotrophic
	Taihu	30	201,807	120.19	31.52	2338	Hypereutrophic
	Chaohu	30	201,508	117.58	31.51	2046	Hypereutrophic
	Weishan	15	201,809	117.17	34.69	1266	Mesotrophic
	Pangong	4	201,607	79.87	33.46	600	Oligotrophic
	Geren	4	201,609	88.54	31.05	476	Oligotrophic
	Cuona	6	201,708	91.431	32.07	400	Oligotrophic
	Xuru	4	201,507	86.46	30.29	300	Oligotrophic
	Fuxian	10	201,509	102.94	24.61	216.5	Oligotrophic
	Jiangcuo	5	201,708	90.79	31.52	200	Oligotrophic
	Maoli	11	201,510	111.94	29.42	38.4	Mesotrophic
	Yangzong	10	201,610	103.01	24.93	31.1	Oligotrophic
	Shanpo	10	201,510	112.03	29.43	26	Mesotrophic

Accuracy assessment

Three evaluation indicators, including the coefficient of determination (R^2), the mean absolute square percentage error (MAPE), and root mean square error (RMSE), were selected to characterize the performance of the model:

$$MAPE = \frac{1}{n}\sum_{i=1}^{n}\left(\left|V^{i}_{meas} - V^{i}_{pred}\right|/V^{i}_{meas}\right) * 100\% \tag{3}$$

$$RMSE = \frac{\sqrt{\sum_{i=1}^{n}\left(V^{i}_{meas} - V^{i}_{pred}\right)^{2}}}{n} \tag{4}$$

where the V^{i}_{pred} and V^{i}_{meas} are the estimated and measured values, respectively; n is the number of samples.

Satellite data collection and preprocessing

A total of 10,523 Sentinel-2 MSI L1C images captured in 410 large waterbodies (areas > 10 km^2) of China were downloaded during the non-freezing period from 2018 to 2021 from the European Space Agency (https://scihub.copernicus.eu/). Because heavy cloud contaminated imagery is unsuitable for Z_{SD} estimation, only imagery with free or low cloud coverages (< 10%) was selected for analysis. These images were atmospherically corrected using Acolite algorithm (Vanhellemont and Ruddick 2014). Water boundaries in the images were extracted following the method described by Zhang et al. (2019). At the same time, Virtual-Baseline Floating macroAlgae Height (VB-FAH) was applied to mask the water pixels with heavy algal blooms (Xing and Hu 2016). During the field studies conducted from 2015 to 2019 (dataset I), the field measured time of a total of 65 points (29 points in Lake Taihu, 12 in Lake Erhai, and 24 points in Lake Wanlv) was close to Sentinel-2 MSI imaging time (± 3 h) and were selected for further validation of the accuracy of Acolite atmospheric correction.

The performance of the Acolite algorithm was assessed by comparing the field measured and Sentinel-2 MSI-derived $R_{rs}(\lambda)$ at the available bands of 443, 490, 560, 665, and 740 nm in the Z_{SD} retrieval algorithm. The field measured $R_{rs}(\lambda)$ were converted to simulated spectrum using the corresponding spectral response functions (SRFs) (Li et al. 2017b; Zeng et al. 2020b), which can be expressed by the following equations:

$$R_{rs}(\lambda) = \sum_{\lambda_{\min}}^{\lambda_{\max}} S_{\lambda} R_{rs\_m}(\lambda) / \sum_{\lambda_{\min}}^{\lambda_{\max}} S_{\lambda} \tag{5}$$

where $R_{rs}(\lambda)$ is the simulation of the Sentinel-2 MSI $R_{rs}(\lambda)$; $\mathrm{R}_{\mathrm{rs\_m}}(\lambda)$ is the field-measured Rrs(λ); and S_λ is the SRF of Sentinel-2 MSI, which can be downloaded from the European Space Agency (https://scihub.copernicus.eu/).

The performance of the Acolite algorithm applied in Sentinel-2 MSI imagery is presented in Fig. S1. The Acolite algorithm had relatively poor performance at blue (443 and 490 nm) wavebands in Lake Taihu, as well as at NIR (740 nm) wavebands in Lake Wanlv, with the MAPE greater than 25%. At the same time, Acolite algorithm performed well in visible wavebands, with the MAPE ranging from 17.06 to 21.1% and the RMSE from 0.001 to 0.009 m. Based on the atmospheric corrected wavebands at visible and NIR bands of Sentinel-2 MSI, i.e., the MAPE values at 443, 490, 560, 665, and 740 nm were less than 30%, and the RMSE values maintained low error values, the Acolite atmospheric correction method is reasonable for these bands and has greater potential in retrieving Z_{SD} based on Sentinel-2 MSI data.

Model development

A new semi-analytical model based on QAA algorithm (Lee et al. 2015, 2016) (denoted as Z_{SD20}) used to estimate Z_{SD} in various waters is proposed in this study. The symbols and corresponding description are summarized in Table S1, and the derivation process in Z_{SD20} algorithm corresponding to various water types is listed in Table 2.

In step 1, $r_{rs}(\lambda)$ could be determined as (Lee et al. 2015, 2016):

$$r_{rs}(\lambda) = \frac{R_{rs}(\lambda)}{0.52 + 1.7R_{rs}(\lambda)} \tag{6}$$

In step 2, $u(\lambda)$ could be expressed as (Lee et al. 2016):

$$u(\lambda) = \frac{-\mathrm{g0} + \sqrt{(\mathrm{g0})^2 + 4\mathrm{g1} * r_{rs}(\lambda)}}{2\mathrm{g}_1} \tag{7}$$

where g0 and g1 was 0.084 and 0.17, respectively, which were suggested by the former study (Lee et al. 1999; Xue et al. 2019).

In step 3, $a(\lambda_0)$ could be determined by making assumption that $a_w\left(\lambda_0\right)$ is domination (Lee et al. 2016; Xue et al. 2019).

$$a\left(\lambda_0\right) = a_w\left(\lambda_0\right) + a_{nw}\left(\lambda_0\right) \tag{8}$$

According to Z_{SDV6} algorithm (Lee et al. 2009), $a\left(\lambda_0\right)$ could be calculated by selecting the reference bands to 560 nm and 670 nm in CW and SW, respectively. Meanwhile, $a\left(\lambda_0\right)$ should be estimated at near infrared region (NIR) in HT, in order to meet an assumed condition that the water absorption $a_w\left(\lambda_0\right)$ dominates in NIR (i.e., $a_w(\mathrm{NIR}) \approx a(\mathrm{NIR})$) (Cai et al. 2023; Rodrigues et al. 2017; Xue et al. 2019). However, such assumptions are not held because the absorption of particulate matter ($a_p(\lambda)$) cannot be ignored in such waters (Le et al. 2009; Zeng et al. 2021), and a large difference may occur between in-situ $a(\mathrm{NIR})$ and $a_w(\mathrm{NIR})$. To fill this gap, we located λ_0 to MSI-740 nm, then estimated $a_{nw}(740)$ from its empirical relationship with $R_{rs}(740)$ based on field-measured data (dataset I, $N = 120$) (Fig. 2a). Therefore, Eq. (8) can be modified as (9):

Table 2 The derivation flowchart of Z_{SD20} algorithm for clear (CW), slightly turbid (ST), and highly turbid waters (HT)

Step	Property	CW	ST	HT
1	$r_{rs}(\lambda)$	$r_{rs}(\lambda) = R_{rs}(\lambda)/(0.52 + 1.7\mathrm{R}_{\mathrm{rs}}(\lambda))$	Same	Same
2	$\mu(\lambda)$	$\mu(\lambda) = \frac{-\mathrm{g}_0 + \left[(\mathrm{g}_0)^2 + 4\mathrm{g}_1 \mathrm{r}_{\mathrm{rs}}(\lambda)\right]^{\frac{1}{2}}}{2\mathrm{g}_1}$ $\mathrm{g}_0 = 0.084, \mathrm{g}_1 = 0.17$	Same	Same
3	$\alpha(\lambda_0)$	$x = \log\left(\frac{r_{rs}(443) + r_{rs}(492)}{r_{rs}(560) + 5\frac{r_{rs}(665)}{r_{rs}(492)} r_{rs}(665)}\right)$ $\alpha(560) = \alpha_w(560) + 10^{-1.146 - 1.366x - 0.469x^2}$	$\alpha\left(\lambda_0\right) = \alpha_w(665) + 0.39\left(\frac{\mathrm{R}_{\mathrm{rs}}(665)}{\mathrm{R}_{\mathrm{rs}}(443) + \mathrm{R}_{\mathrm{rs}}(492)}\right)^{1.14}$	$\alpha\left(\lambda_0\right) \approx \alpha_w(740)$ $+8.14 * R_{rs}(740) + 0.066$
4	$b_b(\lambda_0)$	$b_b\left(\lambda_0\right) = \frac{\mu(\lambda_0)\alpha(\lambda_0)}{1 - \mu(\lambda_0)}$ $\lambda_0 = 560$	Same $\lambda_0 = 665$	Same $\lambda_0 = 740$
5	$b_b(\lambda)$	$b_b(\lambda) = b_b(\lambda_0), \lambda = \lambda_0 = 560$	$b_b(\lambda) = (b_b\left(\lambda_0\right) - b_w\left(\lambda_0\right)) * \left(\frac{\lambda_0}{\lambda}\right)^Y + b_w(\lambda)$ $Y = 3.99 - 3.59\exp(-0.9\frac{r_{rs}(443)}{r_{rs}(560)})$	Same
6	$a(\lambda)$	$a(\lambda) = ((1 - \mu(\lambda))b_b(\lambda)/\mu(\lambda)$	Same	Same
7	$K_d(\lambda)$	$K_d(\lambda) = (1 + 0.0124\theta_w)a(\lambda) + 3.16$ $(1 - 0.52\exp(-10.8 * a(\lambda)))b_b(\lambda)$	Same	Same
8	Z_{SD}	$Z_{SD} = \frac{1}{K_d(\lambda) + K_T(\lambda)}\ln\left(T_r\frac{\lvert r_T - r_W\rvert}{C_t^r}\right)$ $K_T = \left(a + b_b\right)1.04(1 + 5.4u)^{0.5}$	Same	Same

$$a(740) = a_w(740) + 38.14 * R_{rs}(740) + 0.066 \tag{9}$$

In step 4, $b_b(\lambda_0)$ could be expressed as:

$$b_b\left(\lambda_0\right) = \frac{\mu\left(\lambda_0\right)\alpha\left(\lambda_0\right)}{1 - \mu\left(\lambda_0\right)} \tag{10}$$

Furthermore, $b_b(\lambda)$ could be retrieved from $b_b\left(\lambda_0\right)$ as (Lee et al. 2016):

$$b_b(\lambda) = (b_b\left(\lambda_0\right) - b_w\left(\lambda_0\right)) * \left(\frac{\lambda_0}{\lambda}\right)^Y + b_w(\lambda) \tag{11}$$

where the power-law exponent values of $b_b(\lambda)$ (Y) were obtained from different bands ratio as following equations (Xue et al. 2019):

$$Y = 3.99 - 3.59\exp(-0.9\frac{r_{rs}(443)}{r_{rs}(560)}) \tag{12}$$

In step 6, $a(\lambda)$ could be retrieved from $b_b(\lambda)$ as (Lee et al. 2016):

$$a(\lambda) = ((1 - \mu(\lambda))b_b(\lambda)/\mu(\lambda) \tag{13}$$

In step 7, the diffuse attenuation coefficient $K_d(\lambda)$ could be retrieved from $a(\lambda)$ and $b_b(\lambda)$ based on following equation (Lee et al. 2015):

$$K_d(\lambda) = \left(1 + \mathrm{m}_0 * \theta_s\right)a\left(\lambda_0\right) + \mathrm{m}_1(1 - \mathrm{m}_2\exp(-\mathrm{m}_3 a\left(\lambda_0\right)))b_b(\lambda_0) \tag{14}$$

where $K_d(560)$ always represents the minimum K_d value among the transparent spectral domain (443 ~ 665 nm) in the original model (Zeng et al. 2020a); θ_s is the subsurface solar zenith angle; m_{0-3} are model parameters, which were derived using Hydrolight simulations based on oligotrophic waters and Case-1 models of Morel and Maritorena (2001) for optical properties by assuming the IOPs were vertically constant (Lee et al. 2013). Therefore, those parameters (m_{0-3}) should be retuned using in situ data (dataset I) in order to meet the application of inland waters, similar to Lee et al. (2013). In detail, we fixed the same values for m_1, m_2, and m_3, but varied m_0, the optimal value of m_0 was further confirmed based on nonlinear best fit. The values of m_{1-3} were derived in the same way. The retuned values of the four model parameters (m_{0-3}) were 0.012, 3.16, 0.52, and 10.7, respectively. Figure 2b presents the matchup points between the in situ and the retrieved $K_d(560)$ where all of the samples were evenly distributed along the 1:1 line with low MAPE (10.24%) and RMSE (0.81/m), indicating that the new values of the parameters (m_{0-3}) are satisfactory for estimation of $K_d(560)$.

After that, the Z_{SD} is derived based on following equation (Lee et al. 2015):

$$Z_{SD} = \frac{1}{K_d(\lambda) + K_T(\lambda)}\ln\left(T_r\frac{\left|r_T - r_W\right|}{C_t^r}\right) \tag{15}$$

where r_T is the radiance reflectance right above a target and is approximately 0.27/sr (Duntley and Preisendorfer 1952;

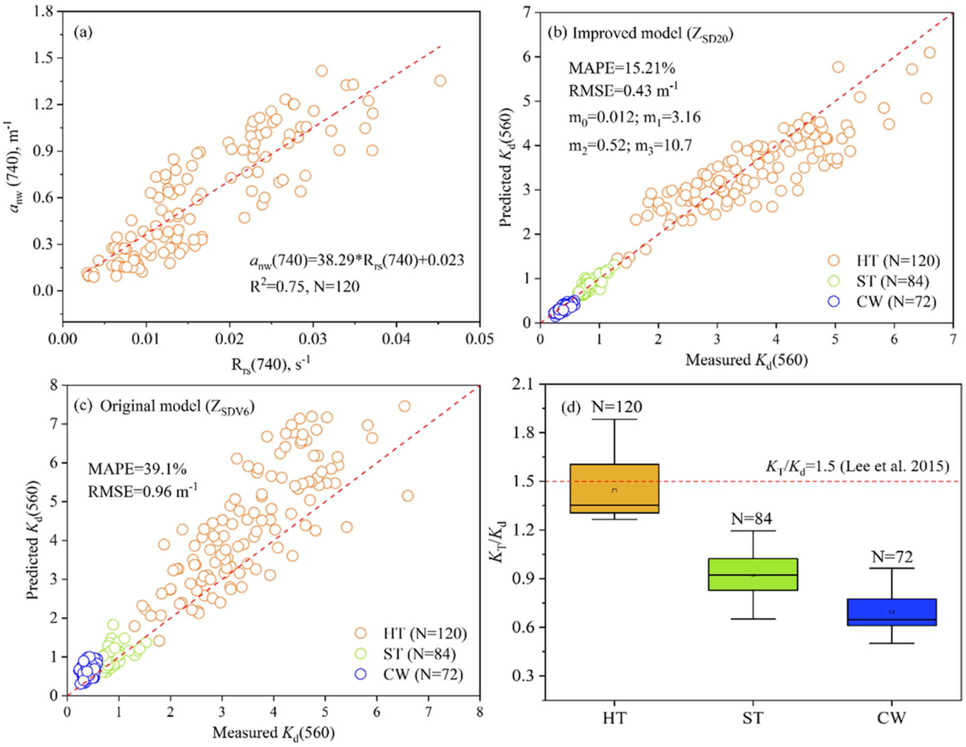

Fig. 2 Relationships between $a_{nm}(740)$ and $R_{rs}(740)$ in highly turbid waters (**a**). The matchup points between the in situ and the retrieved $K_d(560)$ from improved model (**b**) and original model (**c**). The values of K_T/K_d vary in various waters, and the dash line indicated the equation of $K_T/K_d = 1.5$ in original Z_{SDV6} algorithm (**d**)

Lee et al. 2015). The r_W represents the radiance reflectance of water corresponding to the wavelength with K_d, which can be calculated following Eq. (6). The T_r is approximately equal to 0.54/sr, representing the radiance transmittance (Wei et al. 2015). The $C_t^r = 0.013$/sr represents the contrast threshold of what is visible in air (Lee et al. 2015). The K_T is the upward diffuse attenuation coefficient, and the bottom is assumed to be a Lambertian reflector (Lee et al. 2015; Volpe et al. 2011):

$$K_T = \left(a + b_b\right)1.04(1 + 5.4u)^{0.5} = K_d \frac{1.04(1 + 5.4u)^{0.5}}{\left(\frac{1}{1 - \frac{\sin(\theta_s)^2}{RI^2}}\right)^{0.5}} \tag{16}$$

where RI is the refractive index value of pure water, which is equal to an empirical constant of 1.34, and u is defined as $b_b/(a + b_b)$ (Jiang et al. 2019). Therefore, the K_T/K_d only depend on the u when θ_s is confirmed. According to the study of Lee et al. (2015), an empirical equation of $K_T = 1.5K_d$ was determined using a large dataset covering different IOPs, including Case-1 and Case-2 waters. Nevertheless, previous studies found that the value of K_T/K_d can vary and depends on the optical properties (Jiang et al. 2019, Lee et al. 1994, Philpot 1989), which means that the fixed value of K_T/K_d may produce large bias for estimating Z_{SD} in various waters.

According to our field measured data, the values of K_T/K_d showed a wide range (0.5–1.71) in different waters (Fig. 2d), which was different from the empirical constant of 1.5 suggested by Lee et al. (2016). The average values of K_T/K_d were 1.44 in highly turbid (HT), whereas much lower mean values of 0.88 and 0.69 in clear waters (CW) and slightly turbid waters (ST) were found, respectively. Based on the above findings, we can conclude that the new algorithm has satisfying performance in deriving a, K_d, and K_T/K_d in various waters, and it can be applied to identify weaknesses in the original Z_{SDV6} algorithm. According to previous studies (Liu et al. 2020; Xue et al. 2019), the bio-optical properties of inland waters are strongly influenced by the absorption and backscattering of water quality parameters, which are significantly different from the training dataset collected from marine and coastal waters by the original Z_{SDV6} algorithm (Lee et al. 2016). For example, the lakes in Yangtze River Plain cover a wide range of Cchla of 2.48–320.53 mg/L and $a_{CDOM}(440)$ of 0.05–2.18/m (Deyong et al. 2009; Xu et al. 2021b; Zeng et al. 2022a), while relatively small values of Cchla (0.2–40 mg/L) and $a_{CDOM}(440)$ (0.02–0.4/m) were found in the training dataset of original Z_{SDV6} algorithm (Lee et al. 1994). These findings indicated that high dynamic of bio-optical properties (e.g., a and b_b) of inland waters may lead to a wide range of u, K_d, K_T, and ultimately, K_T/K_d. Based on the above analysis, we can conclude that the value of K_T/K_d vary in different waters, and the application of the original Z_{SDV6} algorithm in various waters requires specific parameterization. Therefore, we re-calculated the values of K_T and K_d in the new algorithm following Eqs. (14) and (16).

Results

Biogeochemical characterization

The basic statistics of the field collected water quality parameters in investigated waters are presented in Table S2, comprising a wide variability and covering a wide concentration range of water parameters. The CW have very low C_{Chla} (0.14–19.88 µg/L), $a_{CDOM}(443)$ (0.098–1.01/m), and C_{TSM} (0.47–4.52 mg/L), but high average Z_{SD} value (3.23 m). The ST have moderate C_{Chla} (7.27–34.34 µg/L), $a_{CDOM}(443)$ (0.15–1.87 m^{-1}), and C_{TSM} (1.96–7.5 mg/L). On the contrary, HT is characterized by low water clarity (mean Z_{SD} of 0.43), which closely related to relatively higher C_{Chla} (4.45–30.93 µg/L), $a_{CDOM}(443)$ (0.41–3.78/m), and C_{TSM} (2.5–200.53 mg/L).

Performance of the developed algorithms

Three key improved processes are implemented in the new algorithm. First, suitable reference bands (560 nm, 670 nm, and 740 nm) were available for various waters to estimate the reference total absorption $a\left(\lambda_0\right)$. Secondly, some specific but more accurate parameterization steps of derived K_d were adopted in the new algorithm to reduce defects. Third, more accurate values of K_T/K_d were obtained in the new algorithm. Figure 3 shows the performance of the Z_{SDV6} algorithm (a, b, c, and g) and Z_{SD20} algorithm (d, e, f, and h) in three types of water based on dataset I. The original algorithm may have a moderate performance in CW with a MAPE of 30.86% and an RMSE of 1.28 m (Fig. 3a), which can be improved by using the new developed algorithm with relative higher accuracy (MAPE = 16.88%, RMSE = 0.63 m) (Fig. 3d). At the same time, similar performances were found between the original and new algorithm in water samples dominated by phytoplankton (Fig. S2), which are located in the center of the lake and keep stable deposition condition and are not susceptible to environmental disturbance. In ST and HT, both in non-phytoplankton and phytoplankton-dominated waters, significant underestimations were found for the original algorithm, while the new algorithm performed better (Fig. S2 and Fig. 3). Figure 3g and h summarize the total performance of the original algorithm and our developed algorithm. It can be concluded that the improved algorithm of Z_{SD20} gave more accurate performance, with

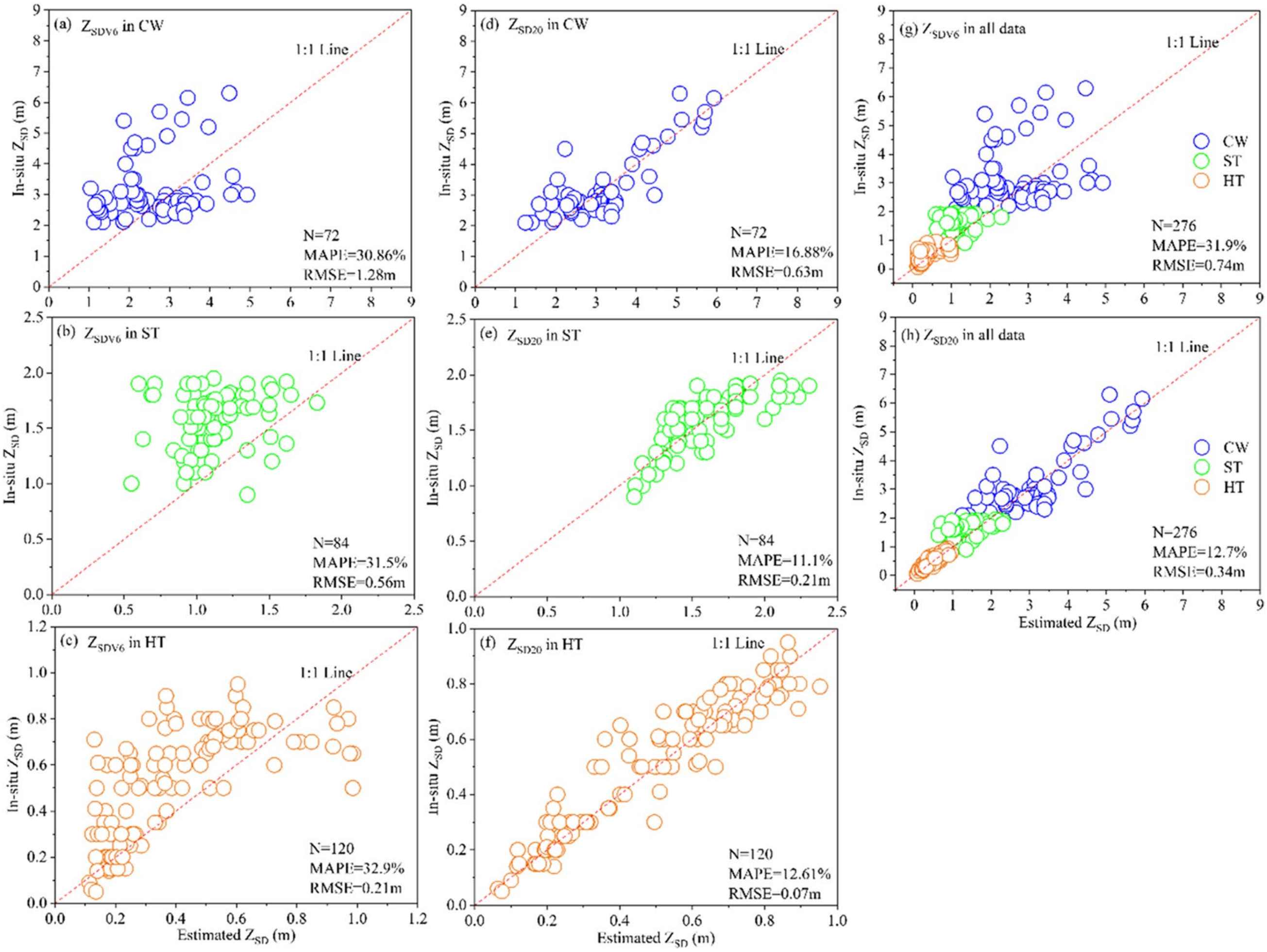

Fig. 3 Performance comparison between Z_{SDV6} algorithm (**a**, **c**, **e**, and **g**) and Z_{SD20} algorithm (**b**, **d**, **f**, and **h**)

value of MAPE reduced from 31.9 to 12.7% and RMSE reduced from 0.74 to 0.34 m.

At the same time, we used dataset II (described in the "The dataset II (validation)" section) as an independent dataset to further test the generality and effectiveness of the proposed algorithm in other waters. The statistical validations are summarized in Table 3. Although an encouraging performance was confirmed using the new algorithm (MAPE = 19.4%, RMSE = 0.67 m), some unsatisfactory results also existed, such as some underestimations of surveyed lakes in Tibet Plateau, which may be related to imperfect atmospheric correction in this area. Regrettably, the field measured spectral data that was closest to Sentinel-2 MSI imaging time was lacking in the examination of the Acolite atmospheric correction. Although these defects were found in our dataset, the new algorithm performed well with satisfactory accuracy and had great potential to further estimate the Z_{SD} in satellite images.

Table 3 The performance of Z_{SD20} in 14 lakes based on validated dataset (dataset II)

Surveyed lakes	In situ mean Z_{SD}	Predicted mean Z_{SD}	MAPE (%)	RMSE (m)
Dongting	0.51	0.49	19.2	0.05
Erhai	0.73	0.69	21	0.06
Taihu	0.5	0.46	17.6	0.04
Chaohu	0.28	0.31	20.5	0.04
Weishan	0.52	0.61	25.3	0.09
Pangong*	3.27	2.45	23.5	0.93
Geren*	3.4	2.69	39.8	2.32
Cuona*	4.6	2.7	36	2.7
Xuru*	4.2	2.62	37.9	2.57
Fuxian	4.6	4.15	17.5	0.52
Jiangcuo*	2.93	2.79	37.1	1.02
Maoli	0.65	0.59	26.9	0.06
Yangzong	2.09	1.94	18.5	0.62
Shanpo	0.37	0.42	25.2	0.05

*Surveyed lakes in Tibetan Plateau

Spatiotemporal variation of water clarity

Seasonal distribution of Z_{SD}

To demonstrate the application of the developed model (Z_{SD20}) in inland waters, we mapped spatiotemporal distribution of Z_{SD} in 410 waters of China, including natural lakes and artificial reservoirs. These waterbodies account for more than 60% of all waterbodies across China with an area more than 10 km^2. The seasonal variations of water clarity in these waterbodies is shown in Fig. 4 and Fig. S3, which shows long-term mean values between 8.24 m (in Lake Yamdrok) and 0.1 m, indicating remarkable spatial and temporal heterogeneity during the observed period (2015–2021), which may be related to different factors among different subregions (Liu et al. 2021a; Shen et al. 2020).

The Z_{SD} of 410 waters across China showed a relatively high Z_{SD} in summer (1.03 ± 1.26 m) and autumn (1.02 ± 1.21 m) but low Z_{SD} in spring (0.69 ± 0.66 m) and winter (0.6 ± 0.72 m), exhibiting a significant temporal variation of water clarity between different seasons (Fig. 4). It was observed that a relatively small seasonal variation of Z_{SD} was found in Huaihe Basin and middle and lower reaches of Yangtze River Plain (HB-MLYRL) (Fig. 5), which may be related to the stable dominant factors in these areas. The waters in these areas always receive major impacts from hydro-climatological events and anthropogenic interference throughout the year, resulting in low water clarity (Song et al. 2020; Wang et al. 2022; Xu et al. 2018b).

At the same time, the seasonal dynamic in proportion of water types was statistically analyzed. The highly turbid waters (HT) always maintain the highest proportion of water types in all seasons (≥ 70%), especially in spring (80%). For slightly turbid waters (ST), the highest percentage was reached in summer, which had a higher proportion of 21% than those in winter (13%), spring (17%), and autumn (19%). The largest proportion of clear waters (CW), accounting for 11% of all waters, were found in autumn, with only 3% and 4% in spring and winter, respectively.

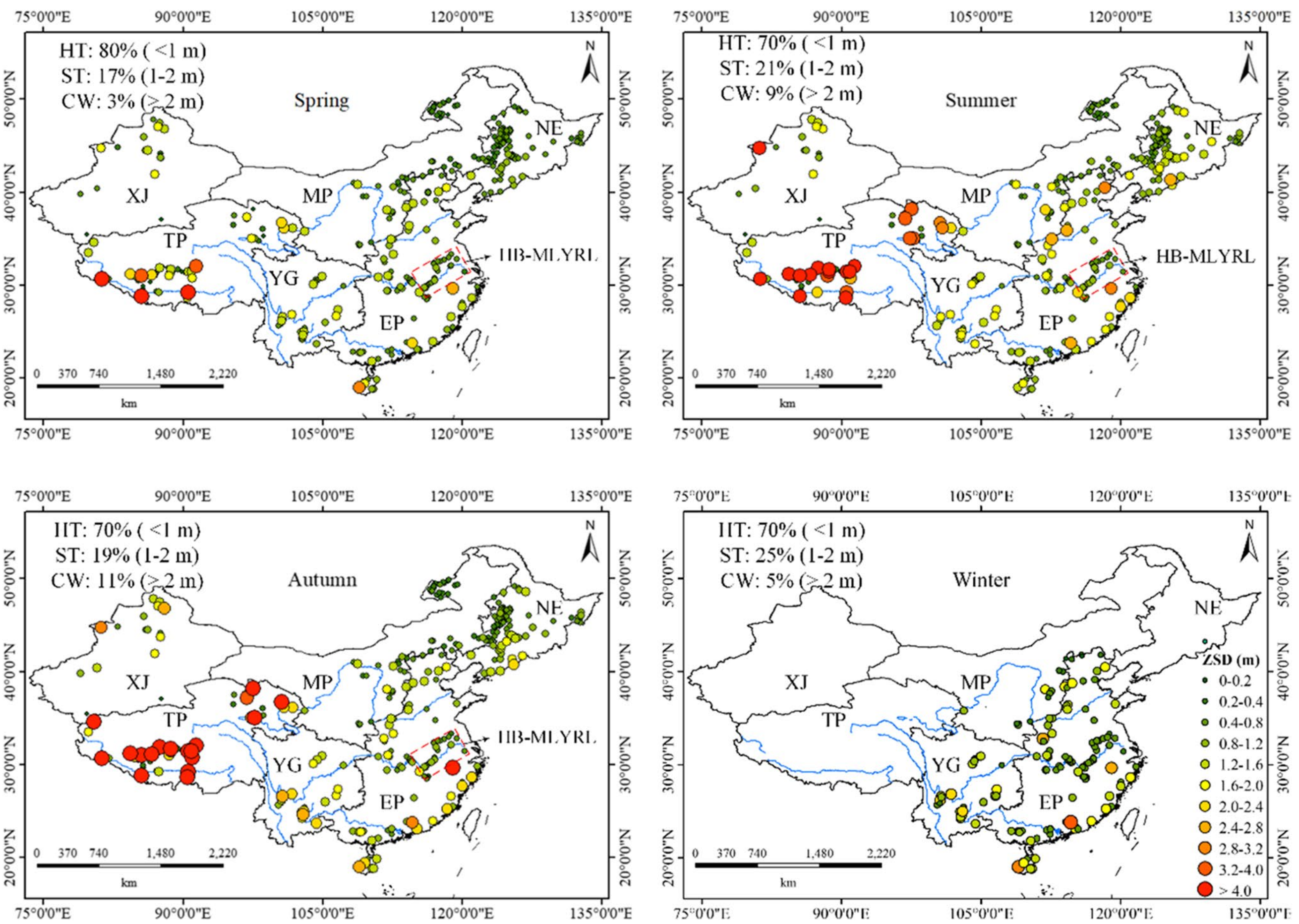

Fig. 4 The seasonal variations of water clarity in lakes of China. The retrieval results of Z_{SD} in some lakes are not shown due to lake freezing period in winter. The waterbodies in Huaihe Basin and middle and lower reaches of Yangtze River Plain (HB-MLYRL) are marked by the dashed rectangle

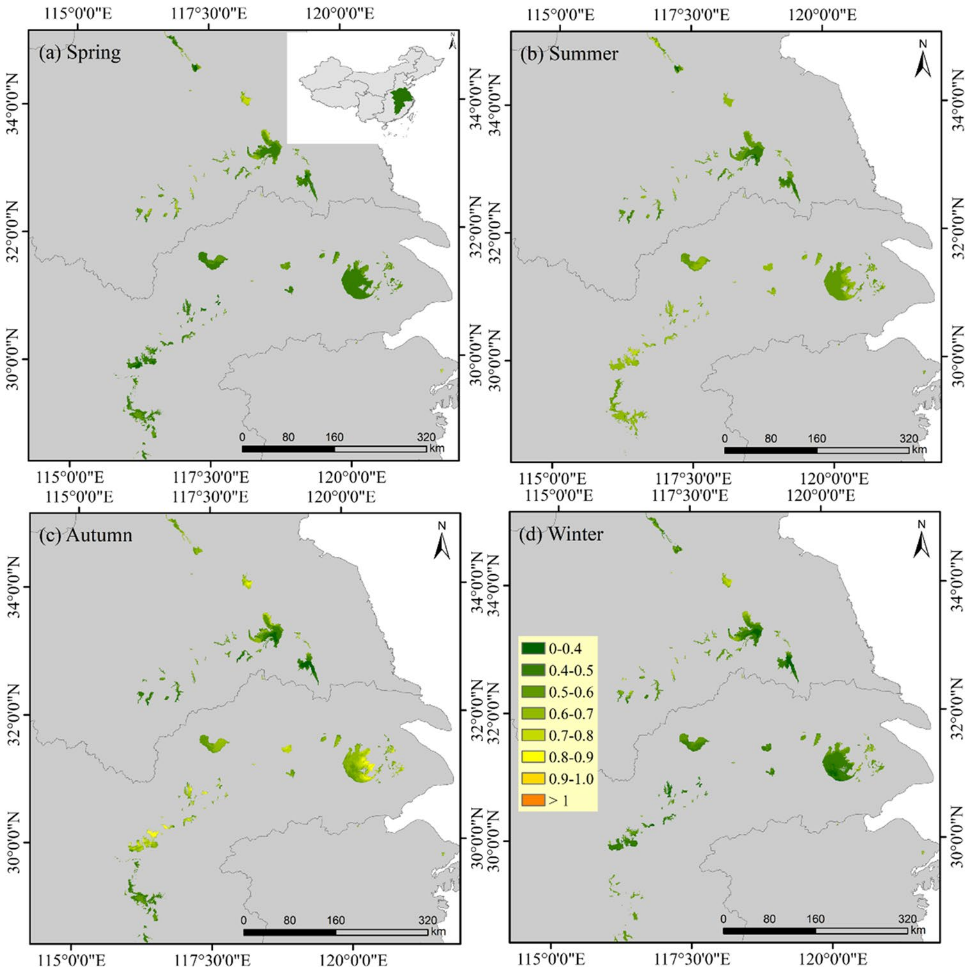

Fig. 5 The seasonal variations of water clarity in Huaihe Basin and middle and lower reaches of Yangtze River Plain (HB-MLYRL)

Spatial distribution of Z_{SD}

For spatial pattern, waterbodies with low Z_{SD} were observed in Eastern China (MP, NE, and EP), where the Z_{SD} ranged from 0.1 to 7.31 m with an average value of 0.25 m (Fig. 6). Most waters in Eastern China are characterized by shallow water depth and highly turbidity, water clarity was influenced by weather conditions and high disturbance from anthropogenic activities (Lei et al. 2020; Song et al. 2020). Conversely, the waters in TP exhibited the highest long-term mean Z_{SD} (2.7 ± 1.4 m), which was much higher than that of all surveyed waters (0.77 ± 0.75 m). The proportion of lakes with different water types is shown in Fig. 4b. Over 50% of lakes in EP, MP, NE, and XJ are characterized by highly turbidity. The largest proportion of CW was found in TP, accounting for 40.98% of all waters, with only 1.64% and 1.67% in MP and NE, respectively. According to previous studies (Liu et al. 2021b; Pi et al. 2020), most waters in TP are characterized by deep water depth (> 15 m), stable deposition condition, and low human disturbance, and are not susceptible environmental disturbance and maintain relatively higher Z_{SD}. In addition, increasing trends of Z_{SD} were found from low–high latitudes and east–west longitudes, indicating that the eutrophic conditions of waters in southern and western China are better than those in northern and eastern China (Fig. 6b), which is consistent with previous findings (Hu et al. 2022; Song et al. 2020). It can be concluded that water clarity exhibited significant spatial variations in China based on the above analysis.

Discussion

Necessity of the improvements in new algorithms

Varied optical active components result in complex bio-optical properties in inland waters characterized by various optical water types. Even at the same phenological period, a single waterbody can also exhibit significant spatially heterogeneous distribution of water optical properties (Matsushita et al. 2015), resulting in the varied performance of Z_{SD} algorithm among those water types. Therefore, the specific optical properties should be considered when applying the Z_{SD} algorithms to various waters.

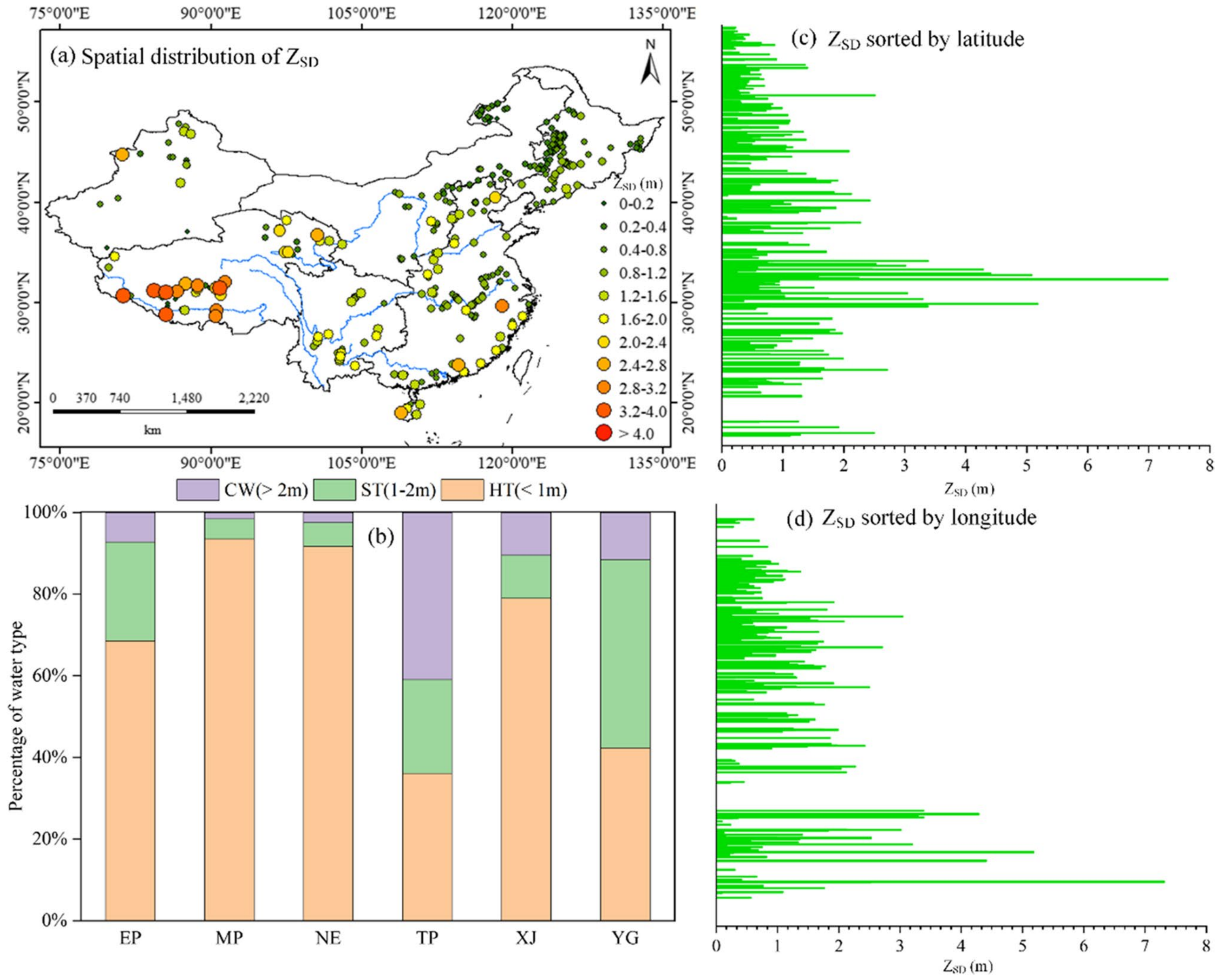

Fig. 6 The spatial distribution in water clarity of 410 waters (**a**), the proportion of various water types in six sub-regions (**b**), with statistical results sorted by latitude (**c**) and longitude (**d**)

In the original algorithm of Z_{SDV6}, the inherent optical properties (IOPs) were first derived based on the QAA algorithm, the Z_{SD} was further derived relying on the minimum K_d value among the transparent spectral domain and its corresponding $R_{rs}(\lambda)$ without parameter adjustments in open ocean and coastal waters (Lee et al. 2016; Shang et al. 2016). Nevertheless, several significant shortages of the original QAA were found for applications in inland waters (Bai et al. 2020; Jiang et al. 2019; Rodrigues et al. 2017). In this study, obvious underestimation of the original algorithm was found in ST (MAPE = 34.3%, RMSE = 0.63 m) with poor performance in CW (MAPE = 30.89%, RMSE = 1.33 m) and HT (MAPE = 36.1%, RMSE = 0.11 m) (Fig. 3) which may be due to the following reasons.

Firstly, the existing estimation algorithm of IOPs at fixed reference wavebands may produce large bias in inland waters due to scattering and absorption (Wang et al. 2017; Watanabe et al. 2016). Therefore, it is necessary to select suitable reference wavebands and bridge the difference between the estimated and field values of total absorption coefficient in various inland waters (Step 3 in Table 2). Additionally, it is possible that the coefficient parameters of derived K_d in the original algorithm were not applicable to inland waters (Watanabe et al. 2016). Therefore, some specific parameterization steps were adopted in the new algorithm to reduce defects (see in Fig. 2). The third issue is that a fixed ratio value of K_T/K_d may lead to an obvious bias estimation in inland waters. In this study, the seasonal values of K_T/K_d in 410 waters across China were derived using data from 2015–2020, which span a wide range of 0.5–1.81 (Fig. 7). It can be seen that the values of K_T/K_d tend to be smaller in clear water (average value of 0.73), slightly turbid waters (1.05), and highly turbid waters (1.47), which is similar to previous study by Jiang et al. (2019). Therefore,

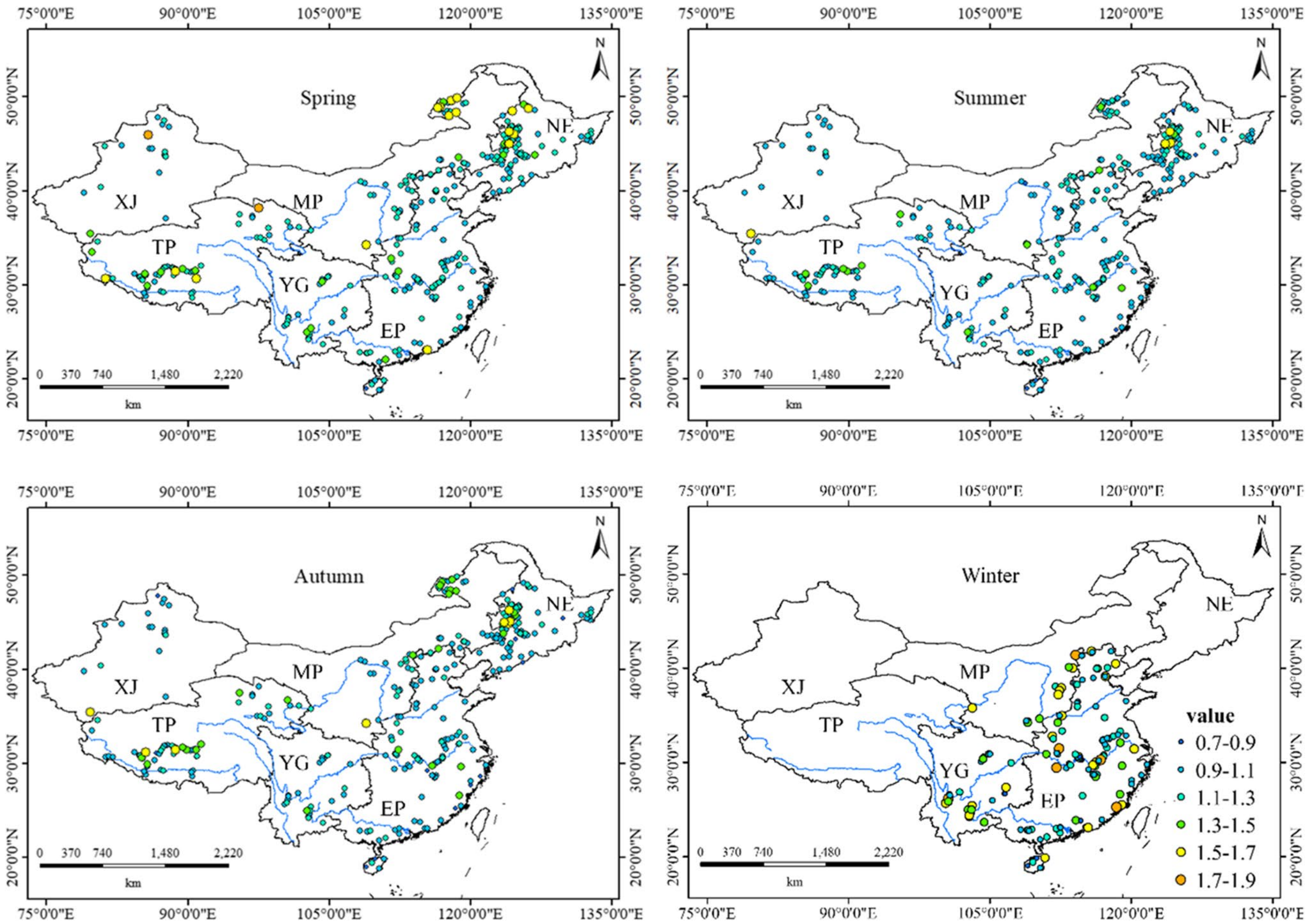

Fig. 7 The seasonal average K_T/K_d in various waters. The retrieval results in winter are not shown due to lake freezing period in winter

improvements are needed in the newly developed algorithm for application in various inland waters. Compared to the native algorithm, three important improvements have been made in the new algorithm. First, a strategy was designed to select suitable reference bands (560 nm, 670 nm, and 740 nm) for various waters to estimate the reference total absorption $a(\lambda_0)$. Secondly, optimized K_d were obtained to reduce defects. Third, more appropriate values of K_T/K_d were implemented in the new algorithm. The validation results indicated that the new algorithm gave more accurate performance, with RMSE reduced from 31.9% to 12.7% and RMSE from 0.74 to 0.34 m (Fig. 3).

Comparison with existing algorithms

A number of empirical and semi-analytical algorithms have been developed to derive Z_{SD} in various waters, covering clear waters to highly turbid waters (Feng et al. 2019; Lee et al. 2016; Mishra et al. 2014; Rodrigues et al. 2017), which were selected for comparison with the algorithm in this study (Table 4). These algorithms can be separated into two groups: the empirical algorithm group (Binding et al. 2015; Giardino et al. 2001; Olmanson et al. 2011; Ren et al. 2018; Wu et al. 2008a, 2008b; Zhang et al. 2021) and the semi-analytical algorithm group (Lee et al. 2016; Rodrigues et al. 2017). However, the performance of these algorithms cannot be directly compared due to the significant differences of band settings in various sensors (e.g., MODIS and Landsat 8). Therefore, all key parameters in the original algorithms must be re-calibrated and validated using the simulated spectrum and field measured datasets.

The performance comparisons between existing algorithms and our algorithm is presented in Table 4. The model of Ren et al. (2018), originally calibrated and validated with data collected from moderate to highly turbid waters, shows relatively higher accuracy (MAPE = 68.44% and RMSE = 0.59 m) compared to others, but a much lower accuracy than the original (MAPE = 21.68% and RMSE = 0.076 m). In contrast, the model of Olmanson et al. (2011) yielded a worse performance than others based on simulated data, with MAPE = 255.91% and RMSE = 4.48 m. Meanwhile, the single band models of Zhang et al. (2021), Wu et al. (2008b), and Binding et al. (2015) also produced relatively poor performance

Table 4 Comparison of performance of dataset II between the existing models and the proposed models

Type	Reference	Equation form	MAPE	RMSE
Empirical	Giardino et al. (2001)	$Z_{SD}=-0.715*(R(560/R(665)))+0.751$	163.01%	1.59 m
	Wu et al. (2008a)	$Z_{SD}=1.133–10.533*R(665)-13.805*(R833)$	73.63%	1.03 m
	Wu et al. (2008b)	$Z_{SD}=\exp(0.76–14.72*R(665))$	115.98%	2.21 m
	Olmanson et al. (2011)	$Z_{SD}=2.29*R(490)/R(665)-16.39*R(490)-0.14$	255.91%	4.88 m
	Binding et al. (2015)	$1/Z_{SD}=0.1701*R(560)^3–0.36*R(560)^2+0.463*R(560)+0.04$	175.7%	1.35 m
	Ren et al. (2018)	$Z_{SD}=1.7351*\exp(-2.141*R(665)/R(560))$	68.44%	0.92 m
	Zhang et al. (2021)	$Z_{SD}=0.0046*R(665)-1.26$	233.56%	3.31 m
Semi-analysis	Lee et al. (2016)	Step1: QAAv6—>$a(\lambda)\&b_b(\lambda)$ Step2: $a(\lambda)\&b_b(\lambda)$—>$K_d(\lambda)$ Step3: $K_d(\lambda)\&\&R_{rs}(\lambda)$—>$Z_{SD}$	31.58%	0.83 m
	Rodrigues et al. (2017)	Step1: QAA_{R17}—>$a(\lambda)\&b_b(\lambda)$ Step2: $a(\lambda)\&b_b(\lambda)$—>$K_d(\lambda)$ Step3: $K_d(\lambda)\&\&R_{rs}(\lambda)$—>$Z_{SD}$	75.89%	1.6 m
	This study	Step1: QAA_{Z20}—>$a(\lambda)\&b_b(\lambda)$ Step2: $a(\lambda)\&b_b(\lambda)$—>$K_d(\lambda)$ Step3: $K_d(\lambda)\&\&R_{rs}(\lambda)$—>$Z_{SD}$	19.4%	0.67 m

based on our validation data. These models are characterized by their simplicity of form and ease of application (Binding et al. 2015; Lei et al. 2020; Zhang et al. 2012). However, the choice of a single band usually varies with the optical properties of the water, developing a generic estimation model for various types of water may produce large uncertainties based on site-specific data (Alikas and Kratzer 2017; Binding et al. 2015; Zhang et al. 2012).

Based on two existing semi-analytical algorithms, significant differences were also observed between the field measured and estimated Z_{SD} after the evaluation of two models from Lee et al. (2016) and Rodrigues et al. (2017) which were carried out based on the same in situ measurements, with MAPE and RMSE of 31.58%, 0.83 m, and 75.89%, 1.6 m, respectively (Table 2), showing poorer accuracy compared to the new proposed models (MAPE = 19.4%, RMSE = 0.67 m). These findings were consistent with previous studies where inadequate performance may occur when these semi-analytical models are applied in turbid inland and coastal waters, such as Lake Taihu, Lake Hongze, Lake Dongting, the Bohai Sea, and the Yellow Sea (Bai et al. 2020; Feng et al. 2019; Jiang et al. 2019; Shang et al. 2016). Although semi-analytical algorithms show greater potential than empirical algorithms for retrieving Z_{SD}, they are also sensitive to errors introduced by different water optical properties (Rodrigues et al. 2017; Yang et al. 2013). Overall, our proposed algorithm showed the best estimation effect when compared to existing algorithms.

Advantage and limitations of the model

The new semi-analytical model was developed on the basis of extensive field measured SDD and Sentinel-2 MSI simulated spectra, and the calibration and validation datasets in the model were collected from different types of water with various dataset over a large geographical area, demonstrating the model's promise for applications in Z_{SD} system assessments on a continental/global scale. Several key wavebands were applied for developing the model, which are also equipped on almost all current earth resource satellites and ocean color satellite platforms (e.g., Sentinel-3, GOCI, and MODIS). The new algorithm performed well with satisfactory accuracy (MAPEs < 39%, RMSEs < 19 m) (Table S3), implying that it had broad applicability for the estimation of Z_{SD} using a variety of satellite data. However, it should be noted that these satellite data may has limited applications in smaller inland waters (e.g., water area < 10 km^2) due to poor spatial resolution (> 250 m).

At the same time, a number of limitations and challenges may stand in the way of practical applications of the proposed method. The atmospheric correction effects are an important factor affecting the accuracy of biochemical parameter retrievals in inland waters (Lei et al. 2019; Ren et al. 2018). In this study, the Acolite model corrected MSI imagery showed promising performance in most visible wavebands, with MAPE < 22% and RMSE < 0.002 (Fig. 2). However, the Acolite model may produce relatively poor performance at blue (443 and 490 nm) wavebands in highly turbid waters, as well as at NIR (740 nm) wavebands in clean waters (Fig. S1). There is no doubt that these negative effects, although the errors remain within permissible limits, could introduce uncertainty into the resulting IOPs and further reduce the final accuracy of the algorithms. Therefore, a reliable estimation of water quality parameters is closely related to the accuracy of corrected spectra, indicating that an excellent atmospheric correction model with high accuracy is necessary.

Furthermore, the bottom effect of shallow water may introduce significant uncertainty on Z_{SD} estimation. For optically deep waters, the upwelling water leaving radiance is regarded as the contributions of water column constituents and the bottom effect can be ignored (Li et al. 2017a, 2018; Wei et al. 2018). However, such assumptions may not hold in optically shallow waters, thus greatly limiting the application of the algorithms. To avoid the reflectance contribution from lake bottom, the new model in this study was calibrated and validated using datasets where euphotic depth is significantly lower than water depth. As there is currently insufficient data to validate whether the constructed algorithms can accurately estimate Z_{SD} in open ocean water or clear waters, caution should be taken when applying the newly developed algorithm under these conditions.

Conclusions

An improved semi-analytical algorithm (Z_{SD20}) was developed for estimating water clarity in various waters with a wide range of water optical properties, which was recalibrated and re-parameterized by our field measured data collected from 16 lakes in China, acquiring a satisfying total performance (MAPE = 19.4%, RMSE = 0.67 m). The algorithm was implemented in 410 waters of China to demonstrate significant spatiotemporal variation of water clarity based on Sentinel-2 MSI imagery from 2018 to 2021. Compared to the native algorithm (Z_{SDV6}), three key improved processes are contained in the new algorithm. First, a strategy was designed to select suitable reference bands (560 nm, 670 nm, and 740 nm) for new algorithm to estimate the reference total absorption $a(\lambda_0)$. Secondly, some specific but more accurate parameterization steps of derived K_d were adopted in the new algorithm to reduce defects. Third, more realistic values of K_T/K_d were implemented in the hybrid algorithm. This study provides a new strategy for estimating water clarity in various waters with a wide range of optical properties, benefitting the monitoring and mitigation of adverse effects on aquatic ecosystems.

Supplementary Information The online version contains supplementary material available at https://doi.org/10.1007/s11356-023-25159-6.

Acknowledgements We thank the European Space Agency for proving Sentinel-2 images. We also gratefully acknowledge the contribution of the editor and two anonymous reviewers for their constructive comments on an early version of this manuscript.

Author contribution Zihong Qin: conceptualization, methodology, software, validation, writing—original draft; Youyue Wen: conceptualization, resources, investigation, funding acquisition; Jiegui Jiang: conceptualization, methodology, software; Qiang Sun: validation, methodology, writing—review and editing, funding acquisition, investigation; all authors read and approved the final manuscript.

Funding This research was supported by the National Science Foundation for Young Scientists of China (42007406), and the Guangzhou Science and Technology Plan Project (No. 202102020666), the Guangdong Natural Science Foundation-General Program (No. 2022A1515010632).

Data availability Data can be made available on request.

Declarations

Ethics approval We declare on behalf that the work described here is original research that has not been published previously, in whole or in part.

Consent to participate All the authors listed consent to participate.

Consent for publication All the authors listed have approved the enclosed manuscript.

Conflict of interest The authors declare no competing interests.

References

Alikas K, Kratzer S (2017) Improved retrieval of Secchi depth for optically-complex waters using remote sensing data. Ecol Ind 77:218–227

Bai S, Gao J, Sun D, Tian M (2020) Monitoring water transparency in shallow and eutrophic lake waters based on GOCI observations. Remote Sens 12(1):163

Balasubramanian SV, Pahlevan N, Smith B, Binding C, Schalles J, Loisel H, Gurlin D, Greb S, Alikas K, Randla M, Bunkei M, Moses W, Nguyễn H, Lehmann MK, O'Donnell D, Ondrusek M, Han T-H, Fichot CG, Moore T, Boss E (2020) Robust algorithm for estimating total suspended solids (TSS) in inland and nearshore coastal waters. Remote Sens Environ 246:111768

Binding CE, Greenberg TA, Watson SB, Rastin S, Gould J (2015) Long term water clarity changes in North America's Great Lakes from multi-sensor satellite observations. Limnol Oceanogr 60(6):1976–1995

Cai X, Li Y, Bi S, Lei S, Xu J, Wang H, Dong X, Li J, Zeng S, Lyu H (2021) Urban water quality assessment based on remote sensing reflectance optical classification. Remote Sens 13(20):4047

Cai X, Li Y, Lei S, Zeng S, Zhao Z, Lyu H, Dong X, Li J, Wang H, Xu J, Zhu Y, Wu L, Cheng X (2023) A hybrid remote sensing approach for estimating chemical oxygen demand concentration in optically complex waters: A case study in inland lake waters in eastern China. Sci Total Environ 856(Pt 1):158869

Carlson RE (1977) A Trophic State Index for Lakes. Limnol Oceanogr 22(2):361–369

Deyong S, Yunmei L, Qiao W (2009) A unified model for remotely estimating chlorophyll a in Lake Taihu, China, based on SVM and in situhyperspectral data. IEEE Trans Geosci Remote Sens 47(8):2957–2965

Duntley S, Preisendorfer R (1952) The visibility of submerged objects

Feng L, Hou X, Zheng Y (2019) Monitoring and understanding the water transparency changes of fifty large lakes on the Yangtze Plain based on long-term MODIS observations. Remote Sens Environ 221:675–686

Fukushima T, Matsushita B, Yang W, Jaelani LM (2017) Semi-analytical prediction of Secchi depth transparency in Lake Kasumigaura using MERIS data. Limnology 19(1):89–100

Giardino C, Pepe M, Brivio PA, Ghezzi P, Zilioli E (2001) Detecting chlorophyll, Secchi disk depth and surface temperature in a sub-alpine lake using Landsat imagery. Sci Total Environ 268(1–3):19–29

Hu M, Ma R, Xiong J, Wang M, Cao Z, Xue K (2022) Eutrophication state in the Eastern China based on Landsat 35-year observations. Remote Sens Environ 277:113057

Jiang D, Matsushita B, Setiawan F, Vundo A (2019) An improved algorithm for estimating the Secchi disk depth from remote sensing data based on the new underwater visibility theory. ISPRS J Photogramm Remote Sens 152:13–23

Le C, Li Y, Zha Y, Sun D, Huang C, Lu H (2009) A four-band semi-analytical model for estimating chlorophyll a in highly turbid lakes: The case of Taihu Lake, China. Remote Sens Environ 113(6):1175–1182

Lee Z, Carder KL, Hawes SK, Steward RG, Davis CO (1994) Model for the interpretation of hyperspectral remote-sensing reflectance. Appl Opt 33(24):5721–5732

Lee Z, Hu C, Shang S, Du K, Lewis M, Arnone R, Brewin R (2013) Penetration of UV-visible solar radiation in the global oceans: insights from ocean color remote sensing. J Geophys Res Oceans 118(9):4241–4255

Lee Z, Shang S, Hu C, Du K, Weidemann A, Hou W, Lin J, Lin G (2015) Secchi disk depth: A new theory and mechanistic model for underwater visibility. Remote Sens Environ 169:139–149

Lee Z, Shang S, Qi L, Yan J, Lin G (2016) A semi-analytical scheme to estimate Secchi-disk depth from Landsat-8 measurements. Remote Sens Environ 177:101–106

Lee Z, Carder KL, Mobley CD, Steward RG, Patch JS (1999) Hyperspectral remote sensing for shallow waters. 2. Deriving bottom depths and water properties by optimization. 38(18): 3831–3843

Lee Z, Lubac B, Werdell J, Arnone R (2009) An update of the quasi-analytical algorithm (QAA_v5)

Lei S, Wu D, Li Y, Wang Q, Huang C, Liu G, Zheng Z, Du C, Mu M, Xu J, Lv H (2018) Remote sensing monitoring of the suspended particle size in Hongze Lake based on GF-1 data. Int J Remote Sens 40(8):3179–3203

Lei S, Xu J, Li Y, Du C, Liu G, Zheng Z, Xu Y, Lyu H, Mu M, Miao S, Zeng S, Xu J, Li L (2019) An approach for retrieval of horizontal and vertical distribution of total suspended matter concentration from GOCI data over Lake Hongze. Sci Total Environ 700:134524

Lei S, Xu J, Li Y, Lyu H, Liu G, Zheng Z, Xu Y, Du C, Zeng S, Wang H, Dong X, Cai X, Li J (2020) Temporal and spatial distribution of Kd(490) and its response to precipitation and wind in lake Hongze based on MODIS data. Ecol Ind 108:105684

Li J, Yu Q, Tian YQ, Becker BL (2017a) Remote sensing estimation of colored dissolved organic matter (CDOM) in optically shallow waters. ISPRS J Photogramm Remote Sens 128:98–110

Li Y, Zhang Y, Shi K, Zhu G, Zhou Y, Zhang Y, Guo Y (2017b) Monitoring spatiotemporal variations in nutrients in a large drinking water reservoir and their relationships with hydrological and meteorological conditions based on Landsat 8 imagery. Sci Total Environ 599–600:1705–1717

Li J, Yu Q, Tian YQ, Becker BL, Siqueira P, Torbick N (2018) Spatio-temporal variations of CDOM in shallow inland waters from a semi-analytical inversion of Landsat-8. Remote Sens Environ 218:189–200

Li Y, Shi K, Zhang Y, Zhu G, Zhang Y, Wu Z, Liu M, Guo Y, Li N (2020) Analysis of water clarity decrease in Xin'anjiang Reservoir, China, from 30-Year Landsat TM, ETM+, and OLI observations. J Hydrol 590:125476

Liu G, Li L, Song K, Li Y, Lyu H, Wen Z, Fang C, Bi S, Sun X, Wang Z, Cao Z, Shang Y, Yu G, Zheng Z, Huang C, Xu Y, Shi K (2020) An OLCI-based algorithm for semi-empirically partitioning absorption coefficient and estimating chlorophyll a concentration in various turbid case-2 waters. Remote Sens Environ 239:111648

Liu C, Zhu L, Li J, Wang J, Ju J, Qiao B, Ma Q, Wang S (2021a) The increasing water clarity of Tibetan lakes over last 20 years according to MODIS data. Remote Sens Environ 253:112199

Liu G, Li S, Song K, Wang X, Wen Z, Kutser T, Jacinthe PA, Shang Y, Lyu L, Fang C, Yang Y, Yang Q, Zhang B, Cheng S, Hou J (2021b) Remote sensing of CDOM and DOC in alpine lakes across the Qinghai-Tibet Plateau using Sentinel-2A imagery data. J Environ Manage 286:112231

Matsushita B, Yang W, Yu G, Oyama Y, Yoshimura K, Fukushima T (2015) A hybrid algorithm for estimating the chlorophyll-a concentration across different trophic states in Asian inland waters. ISPRS J Photogramm Remote Sens 102:28–37

Mishra S, Mishra DR, Lee Z (2014) Bio-optical inversion in highly turbid and cyanobacteria-dominated waters. IEEE Trans Geosci Remote Sens 52(1):375–388

Morel A, Maritorena S (2001) Bio-optical properties of oceanic waters: A reappraisal. J Geophys Res Oceans 106(C4):7163–7180

Mu M, Li Y, Bi S, Lyu H, Xu J, Lei S, Miao S, Zeng S, Zheng Z, Du C (2021) Prediction of algal bloom occurrence based on the naive Bayesian model considering satellite image pixel differences. Ecol Ind 124:107416

Olmanson LG, Brezonik PL, Finlay JC, Bauer ME (2016) Comparison of Landsat 8 and Landsat 7 for regional measurements of CDOM and water clarity in lakes. Remote Sens Environ 185:119–128

Olmanson LG, Brezonik PL, Bauer ME (2011) Evaluation of medium to low resolution satellite imagery for regional lake water quality assessments. Water Resour Res 47(9)

Philpot WD (1989) Bathymetric mapping with passive multispectral imagery. Appl Opt 28(8):1569–1578

Pi X, Feng L, Li W, Zhao D, Kuang X, Li J (2020) Water clarity changes in 64 large alpine lakes on the Tibetan Plateau and the potential responses to lake expansion. ISPRS J Photogramm Remote Sens 170:192–204

Ren J, Zheng Z, Li Y, Lv G, Wang Q, Lyu H, Huang C, Liu G, Du C, Mu M, Lei S, Bi S (2018) Remote observation of water clarity patterns in Three Gorges Reservoir and Dongting Lake of China and their probable linkage to the Three Gorges Dam based on Landsat 8 imagery. Sci Total Environ 625:1554–1566

Rodrigues T, Alcântara E, Watanabe F, Imai N (2017) Retrieval of Secchi disk depth from a reservoir using a semi-analytical scheme. Remote Sens Environ 198:213–228

Shang S, Lee Z, Shi L, Lin G, Wei G, Li X (2016) Changes in water clarity of the Bohai Sea: Observations from MODIS. Remote Sens Environ 186:22–31

Shen M, Duan H, Cao Z, Xue K, Qi T, Ma J, Liu D, Song K, Huang C, Song X (2020) Sentinel-3 OLCI observations of water clarity in large lakes in eastern China: Implications for SDG 6.3.2 evaluation. Remote Sens Environ 247:111950

Shi K, Zhang Y, Zhu G, Qin B, Pan D (2018) Deteriorating water clarity in shallow waters: Evidence from long term MODIS and in-situ observations. Int J Appl Earth Obs Geoinf 68:287–297

Song K, Ma J, Wen Z, Fang C, Shang Y, Zhao Y, Wang M, Du J (2017) Remote estimation of Kd (PAR) using MODIS and Landsat imagery for turbid inland waters in Northeast China. ISPRS J Photogramm Remote Sens 123:159–172

Song K, Liu G, Wang Q, Wen Z, Lyu L, Du Y, Sha L, Fang C (2020) Quantification of lake clarity in China using Landsat OLI imagery data. Remote Sens Environ 243:111800

Song K, Wang Q, Liu G, Jacinthe PA, Li S, Tao H, Du Y, Wen Z, Wang X, Guo W, Wang Z, Shi K, Du J, Shang Y, Lyu L, Hou J, Zhang B, Cheng S, Lyu Y, Fei L (2021) A unified model for high resolution mapping of global lake (>1 ha) clarity using Landsat imagery data. Sci Total Environ 151188

Vanhellemont Q, Ruddick K (2014) Turbid wakes associated with offshore wind turbines observed with Landsat 8. Remote Sens Environ 145:105–115

Volpe V, Silvestri S, Marani M (2011) Remote sensing retrieval of suspended sediment concentration in shallow waters. Remote Sens Environ 115(1):44–54

Wang Y, Shen F, Sokoletsky L, Sun X (2017) Validation and calibration of QAA algorithm for CDOM absorption retrieval in the Changjiang (Yangtze) estuarine and coastal waters. Remote Sensing 9(11):1192

Wang H, Li Y, Zeng S, Cai X, Bi S, Liu H, Mu M, Dong X, Li J, Xu J, Lyu H, Zhu Y, Zhang Y (2022) Recognition of aquatic vegetation above water using shortwave infrared baseline and phenological features. Ecol Ind 136:108607

Watanabe F, Mishra DR, Astuti I, Rodrigues T, Alcântara E, Imai NN, Barbosa C (2016) Parametrization and calibration of a quasi-analytical algorithm for tropical eutrophic waters. ISPRS J Photogramm Remote Sens 121:28–47

Wei J, Lee Z, Lewis M, Pahlevan N, Ondrusek M, Armstrong R (2015) Radiance transmittance measured at the ocean surface. Opt Express 23(9):11826–11837

Wei J, Lee Z, Garcia R, Zoffoli L, Armstrong RA, Shang Z, Sheldon P, Chen RF (2018) An assessment of Landsat-8 atmospheric correction schemes and remote sensing reflectance products in coral reefs and coastal turbid waters. Remote Sens Environ 215:18–32

Wu G, de Leeuw J, Liu Y (2008a) Understanding seasonal water clarity dynamics of lake dahuchi from in situ and remote sensing data. Water Resour Manage 23(9):1849–1861

Wu G, De Leeuw J, Skidmore AK, Prins HHT, Liu Y (2008b) Comparison of MODIS and Landsat TM5 images for mapping tempo–spatial dynamics of Secchi disk depths in Poyang Lake National Nature Reserve. China International Journal of Remote Sensing 29(8):2183–2198

Xing Q, Hu C (2016) Mapping macroalgal blooms in the Yellow Sea and East China Sea using HJ-1 and Landsat data: Application of a virtual baseline reflectance height technique. Remote Sens Environ 178:113–126

Xu J, Fang C, Gao D, Zhang H, Gao C, Xu Z, Wang Y (2018a) Optical models for remote sensing of chromophoric dissolved organic matter (CDOM) absorption in Poyang Lake. ISPRS J Photogramm Remote Sens 142:124–136

Xu J, Jin G, Tang H, Zhang P, Wang S, Wang Y-G, Li L (2018b) Assessing temporal variations of Ammonia Nitrogen concentrations and loads in the Huaihe River Basin in relation to policies on pollution source control. Sci Total Environ 642:1386–1395

Xu J, Lei S, Bi S, Li Y, Lyu H, Xu J, Xu X, Mu M, Miao S, Zeng S, Zheng Z (2020) Tracking spatio-temporal dynamics of POC sources in eutrophic lakes by remote sensing. Water Res 168:115162

Xu H, Xu G, Wen X, Hu X, Wang Y (2021a) Lockdown effects on total suspended solids concentrations in the Lower Min River (China) during COVID-19 using time-series remote sensing images. Int J Appl Earth Obs Geoinf 98:102301

Xu J, Bian Y, Lyu H, Miao S, Li Y, Liu H, Xu J (2021b) Estimation of particulate backscattering coefficient in turbid inland water using Sentinel 3A-OLCI image. IEEE J Sel Top Appl Earth Obs Remote Sens 14:8577–8593

Xu J, Li Y, Lyu H, Lei S, Mu M, Bi S, Xu J, Xu X, Miao S, Li L, Yan X (2021c) Simultaneous inversion of concentrations of POC and its endmembers in lakes: a novel remote sensing strategy. Sci Total Environ 770:145249

Xue K, Ma R, Duan H, Shen M, Boss E, Cao Z (2019) Inversion of inherent optical properties in optically complex waters using sentinel-3A/OLCI images: a case study using China's three largest freshwater lakes. Remote Sens Environ 225:328–346

Yang W, Matsushita B, Chen J, Yoshimura K, Fukushima T (2013) Retrieval of Inherent Optical Properties for Turbid Inland Waters From Remote-Sensing Reflectance. IEEE Trans Geosci Remote Sens 51(6):3761–3773

Zeng S, Lei S, Li Y, Lyu H, Xu J, Dong X, Wang R, Yang Z, Li J (2020a) Retrieval of Secchi disk depth in turbid lakes from GOCI based on a new semi-analytical algorithm. Remote Sens 12(9):1516

Zeng S, Li Y, Lyu H, Xu J, Dong X, Wang R, Yang Z, Li J (2020b) Mapping spatio-temporal dynamics of main water parameters and understanding their relationships with driving factors using GF-1 images in a clear reservoir. Environ Sci Pollut Res Int 27(27):33929–33950

Zeng S, Lei S, Li Y, Lyu H, Dong X, Li J, Cai X (2021) Remote monitoring of total dissolved phosphorus in eutrophic Lake Taihu based on a novel algorithm: Implications for contributing factors and lake management. Environ Pollut 296:118740

Zeng S, Du C, Li Y, Lyu H, Dong X, Lei S, Li J, Wang H (2022a) Monitoring the particulate phosphorus concentration of inland waters on the Yangtze Plain and understanding its relationship with driving factors based on OLCI data. Sci Total Environ 809:151992

Zeng S, Lei S, Li Y, Lyu H, Dong X, Li J, Cai X (2022b) Remote monitoring of total dissolved phosphorus in eutrophic Lake Taihu based on a novel algorithm: Implications for contributing factors and lake management. Environ Pollut 296:118740

Zhang G, Yao T, Chen W, Zheng G, Shum CK, Yang K, Piao S, Sheng Y, Yi S, Li J, O'Reilly CM, Qi S, Shen SSP, Zhang H, Jia Y (2019) Regional differences of lake evolution across China during 1960s–2015 and its natural and anthropogenic causes. Remote Sens Environ 221:386–404

Zhang Y, Zhang Y, Shi K, Zhou Y, Li N (2021) Remote sensing estimation of water clarity for various lakes in China. Water Res 192:116844

Zhang Y, Liu X, Yin Y, Wang M, Qin B (2012) A simple optical model to estimate diffuse attenuation coefficient of photosynthetically active radiation in an extremely turbid lake from surface reflectance. 20(18): 20482-20493

Zhao D, Cai Y, Jiang H, Xu D, Zhang W, An S (2011) Estimation of water clarity in Taihu Lake and surrounding rivers using Landsat imagery. Adv Water Resour 34(2):165–173

Zheng Z, Ren J, Li Y, Huang C, Liu G, Du C, Lyu H (2016) Remote sensing of diffuse attenuation coefficient patterns from Landsat 8 OLI imagery of turbid inland waters: a case study of Dongting Lake. Sci Total Environ 573:39–54